

# Measuring full counting statistics in a quantum simulator

Lata Kh Joshi,<sup>1</sup> Filiberto Ares,<sup>1</sup> Manoj K. Joshi,<sup>2,3</sup> Christian F. Roos,<sup>2,3</sup> and Pasquale Calabrese<sup>1,4</sup>

<sup>1</sup>*SISSA and INFN, via Bonomea 265, 34136 Trieste, Italy*

<sup>2</sup>*Institute for Quantum Optics and Quantum Information, Austrian Academy of Sciences, Technikerstraße 21a, 6020 Innsbruck, Austria*

<sup>3</sup>*University of Innsbruck, Institute for Experimental Physics, Technikerstraße 25, 6020 Innsbruck, Austria*

<sup>4</sup>*International Centre for Theoretical Physics (ICTP), Strada Costiera 11, 34151 Trieste, Italy*

In quantum mechanics, the probability distribution function (PDF) and full counting statistics (FCS) play a fundamental role in characterizing the fluctuations of quantum observables, as they encode the complete information about these fluctuations. In this letter, we measure these two quantities in a trapped-ion quantum simulator for the transverse and longitudinal magnetization within a subsystem. We utilize the toolbox of classical shadows to postprocess the measurements performed in random bases. The measurement scheme efficiently allows access to the FCS and PDF of all possible operators on desired choices of subsystems of an extended quantum system.

*Introduction*— One of the most striking and fundamental features of quantum mechanics is that the result of a measurement is inherently random. Thus the complete characterization of an observable requires to know the Probability Distribution Function (PDF) of the possible measurement outcomes or, alternatively, the Full Counting Statistics (FCS), the cumulant generating function of the PDF. These quantities encode all the information about the quantum fluctuations of an observable. Understanding such fluctuations is not only essential at a fundamental level but also finds important applications in, for example, the development of optical and electrical devices [1–3], atomic and particle physics [4, 5], random number generation [6], and materials science [7], to name a few.

In many-body quantum systems, there is a growing interest in the study of PDFs and FCS. The progresses in quantum simulators have allowed to access them experimentally in various setups [8–13]. These experiments consider either local observables, defined on a single point, or global ones, with support on the entire system. On the other hand, the recent theoretical effort has focused on observables defined on extended subsystems. In this case, the FCS not only exhibits universal signatures both in [14–31] and out-of [32–44] equilibrium, where it can be used as a probe of relaxation and thermalization, but is also closely related to other key quantities such as entanglement entropies [45–53]. In fact, the FCS is the simplest example of a broader class of specialized partition functions known as charged moments. These charged moments allow one to resolve the entanglement by decomposing it across the different symmetry sectors of the system [54–56] and to quantify the degree a symmetry is broken in a subsystem [57, 58]. Although there is a large number of theoretical works, only very recently the non-equilibrium particle number PDF in an extended spatial region has been experimentally probed in a quantum gas microscope [59] and in superconducting quantum magnets [60]. In particular, the latter work employs the FCS to falsify some conjectures on the dynamical universality of Heisenberg spin chains, highlighting the relevance of studying quantum fluctuations beyond the

first fewer cumulants, see also [61, 62].

In the present work, we measure time-evolved PDFs and FCS after a sudden quench in an ion-trap quantum simulator, reanalyzing randomized measurement data from Refs. [63] and [64]. We consider as observables the magnetization on a block of ions both along the transverse ( $z$ ) and the longitudinal ( $x$ ) axes. While the former magnetization is globally conserved by our simulated dynamics, it is not the case in the latter one. The theoretical calculation of the subsystem FCS of a non-conserved global observable is a challenging task, even in the simplest and most paradigmatic situations [17, 24, 34, 35, 37]. This is one of the main reasons why previous experimental studies, as well as the majority of theoretical investigations, have been limited to globally conserved quantities. The randomized measurement protocol instead allows us to access the FCS and the PDF of any subsystem observable, whether or not it is globally conserved under the time evolution.

*Full Counting Statistics and Probability Distribution Functions*— Let us consider an extended quantum system in a state  $|\Psi\rangle$  and divide it into two spatial parts  $A$  and  $\bar{A}$ . We take a quantum observable  $O$  which can be decomposed into the contributions from  $A$  and  $\bar{A}$  as  $O = O_A + O_{\bar{A}}$ . The FCS of  $O_A$  is

$$\chi(\alpha) = \text{Tr}(\rho_A e^{i\alpha O_A}), \quad (1)$$

where  $\rho_A = \text{Tr}_{\bar{A}}(|\Psi\rangle\langle\Psi|)$  is the reduced density matrix of the subsystem  $A$ . The derivatives of (1) with respect to the spectral parameter  $\alpha \in [0, 2\pi]$  at  $\alpha = 0$  give access to the moments of  $O_A$ . The probability  $p(q)$  of obtaining a value  $q$  in a measurement of  $O_A$  is

$$p(q) = \text{Tr}(\Pi_q \rho_A), \quad (2)$$

where  $\Pi_q$  is the projector onto the eigenspace of  $O_A$  associated with the eigenvalue  $q$ .

As is evident from the definition, the FCS is in general a complex number. In particular, the imaginary part of  $\chi(\alpha)$  is a direct probe of how asymmetric the PDF is with respect to  $q = 0$ . When  $\text{Im}[\chi(\alpha)] = 0$ , the PDF follows  $p(q) = p(-q)$ . Furthermore, the slope of this imaginary

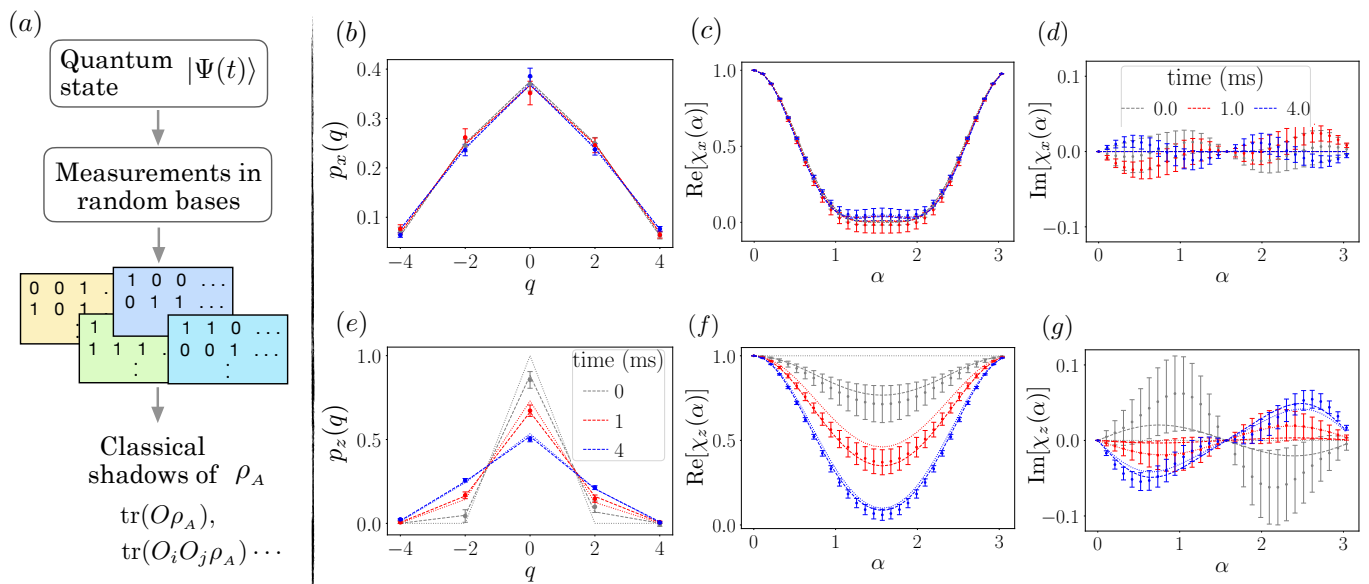


FIG. 1: a) *Protocol to measure operator expectation values using classical shadows*: The protocol used to measure the full counting statistics (FCS) and the probability distribution function (PDF) of an observable  $O$  in a subsystem  $A$  is based on collecting randomized shadows of the reduced density matrix  $\rho_A$ . The quantum system is prepared in the desired state  $|\Psi(t)\rangle$ . The final measurements are obtained in uniformly distributed random bases. Experimental repetitions with various random bases and shots provide access to the FCS and PDF. The total system size is  $N = 10$  ions and the subsystem, of size  $N_A = 4$ , is chosen from the central sites of the chain. (b, e) *Magnetization PDFs in a quench from the Néel state*: We utilize the experimental data from Ref. [63] to extract the PDF  $p_x(q)$ , of the longitudinal magnetization  $S_A^x$ , and the PDF  $p_z(q)$ , of the transverse magnetization  $S_A^z$  at different times. (c, d, f, g) *Magnetization FCS in a quench from the Néel state*: The real and imaginary parts of the FCS of  $S_A^x$  (in (c) and (d)) and that of  $S_A^z$  (in (f) and (g)) are shown. As a proof of principle, the experiment perfectly captures the expected behavior for the PDF and FCS (see main text for details). In all the panels different colors correspond to three different times;  $t = 0$  ms in gray,  $t = 1$  ms in red, and  $t = 4$  ms in blue. The dotted lines show the theoretical prediction for a perfect Néel state whereas the dashed lines are the prediction for an initial Néel state corrected for bit-flip errors. Symbols and error bars show the experimental data.

part at  $\alpha = 0$  is the operator expectation value, i.e.,  $d\text{Im}[\chi(\alpha)]/d\alpha|_{\alpha=0} = \langle O_A \rangle$ , which is also the mean of the PDF. From the real part of the FCS, we can infer  $\langle O_A^2 \rangle$ , which is the curvature of  $\text{Re}[\chi(\alpha)]$  at  $\alpha = 0$ , whereas the variance of the PDF, i.e.,  $\sigma^2 = \langle O_A^2 \rangle - \langle O_A \rangle^2$ , can be directly obtained from the logarithm of the FCS (more details in Appendix A).

Our experimental protocol to measure the FCS and PDF builds on the versatile randomized measurement toolbox [65, 66]. The quantum system of  $N$  qubits is prepared in a particular configuration  $|\Psi_0\rangle$  and then is quenched with the engineered Hamiltonian  $H$  to reach the time evolved state  $|\Psi(t)\rangle$ , see, e.g., Refs. [63, 64]. As summarized in Fig. 1 (a), on this state measurements are performed in random bases. For each random basis, the experiment is repeated to collect quantum projections, which are then used to obtain shadows of the time-evolved state (see Appendix B for details of the protocol and estimators). Such experiments were recently performed in various setups and have been useful to access fundamental non-equilibrium properties of quantum systems, from entanglement entropies in pure [63, 67–

70] and mixed states [71–73], rate of information scrambling [74] to quantum chaos [75, 76]. In this letter, we use the experimental data obtained using the above protocol from Refs. [63, 64]. These references study the time evolution of the Rényi entanglement entropy after a quench from the Néel state [63] and the dynamical restoration of broken symmetries in tilted ferromagnetic states [64]. The key new element in our work is the post-processing of the experimental data to access the FCS and PDFs in these experiments.

*Setup*— The experiment we use is a quantum simulator based on trapped  $\text{Ca}^+$  ions. The qubit basis states, labeled by the vectors  $s = (|\downarrow\rangle, |\uparrow\rangle) \equiv (1, 0)$ , are encoded into the  $|S_{1/2}, m = +1/2\rangle$  and  $|D_{5/2}, m = +5/2\rangle$  electronic levels of the ions. We consider two sets of initial states, both of which are quenched with an engineered power-law decaying XY Hamiltonian

$$H_{\text{XY}} = \sum_{i>j} \frac{J_0}{2|i-j|^\alpha} (\sigma_i^x \sigma_j^x + \sigma_i^y \sigma_j^y), \quad (3)$$

where  $\sigma_i^a$  are the spin-1/2 Pauli matrices for  $a = x, y$  at the lattice site  $i = 1 \dots N$ . We study two cases from

two independent runs of the experiment: **I**) In the first case, as in Ref. [63], the initial state is a Néel state,  $|\Psi_0\rangle = |\uparrow\downarrow\uparrow\downarrow\dots\rangle$ , in a total system of  $N = 10$  spins. The interaction strength ( $J_0$ ) and range ( $\alpha$ ) in the quenching Hamiltonian are  $J_0 \approx 420$  rad/s and  $\alpha \approx 1.24$ , respectively; **II**) In the second case, as in Ref. [64], the initial state is a tilted ferromagnet, i.e., a ferromagnetic state  $|\downarrow\downarrow\downarrow\dots\rangle$  rotated by an angle  $\theta$  away from the  $z$ -axis,

$$|\Psi_0(\theta)\rangle = e^{i\frac{\theta}{2}\sum_j\sigma_j^y}|\downarrow\downarrow\downarrow\dots\rangle. \quad (4)$$

The total system size studied is  $N = 12$  spins with the parameters in the quenching Hamiltonian being  $J_0 \approx 560$  rad/s and  $\alpha \approx 1$ .

For the purpose of the illustration, in the present work, we measure the FCS  $\chi_\mu(\alpha)$  and PDF  $p_\mu(q)$  of  $S_A^\mu = \sum_{j \in A} \sigma_j^\mu$ , which are the transverse ( $\mu = z$ ) and longitudinal ( $\mu = x$ ) magnetization in a subsystem  $A$ . Note that we have defined  $S_A^z$  and  $S_A^x$  as twice the usual magnetizations in order that their eigenvalues are integers. The full system transverse magnetization is conserved by the post-quench Hamiltonian, i.e.  $[S_{A+\bar{A}}^z, H_{XY}] = 0$ , but the longitudinal one is not,  $[S_{A+\bar{A}}^x, H_{XY}] \neq 0$ . The FCS of both magnetizations satisfies  $\chi_\mu(\alpha + k\pi) = (-1)^{kN_A} \chi_\mu(\alpha)$  where  $k \in \mathbb{Z}$  and  $N_A$  is the number of spins in  $A$ . Therefore,  $\chi_\mu(\alpha)$  is a periodic function of period  $\pi$  ( $2\pi$ ) for subsystems with an even (odd) number of sites.

*Case I: Probability distribution function and full counting statistics in the quench dynamics of the Néel state–*

In Fig. 1 (b), we present the PDF of the longitudinal magnetization  $S_A^x$  at times  $t = 0$  ms (in gray), 1 ms (in red) and 4 ms (in blue) in a system of 10 ions and subsystem of size  $N_A = 4$ . In the initial Néel state, we expect  $p_x(q) = 2^{-N_A} \binom{N_A}{(N_A-q)/2}$ . We obtain a good match between the theoretical prediction (dashed curve) and the experimental data (dots and error bars). We notice that, under the quench dynamics, the PDF  $p_x(q)$  changes slightly with time and remains symmetric around the eigenvalue  $q = 0$ . This is further confirmed by the measurements of the corresponding FCS  $\chi_x(\alpha)$  presented in Fig. 1 (c-d). Theoretically, for an initial Néel state, the FCS of  $S_A^x$  at  $t = 0$  is  $\chi_x(\alpha) = \cos^{N_A} \alpha$ . The imaginary part remains zero within error bars at all times. After the quench with the XY Hamiltonian (3),  $\langle S_A^x \rangle = 0$  at all times, which agrees with the zero slope of the imaginary FCS at  $\alpha = 0$ . Interestingly, the curvature of the real part of FCS at  $\alpha = 0$ , i.e.  $\langle (S_A^x)^2 \rangle$ , coincides with the variance of the PDF in the present case since  $\langle S_A^x \rangle = 0$ . Thus, in Figs. 1 (b) and (c), the change of the variance of the PDF with time is exactly the same as the change of the curvature of the real part of the FCS. In Appendix C, we show  $\langle (S_A^x)^2 \rangle$  as a function of time.

As stated in the introduction, the same experimental dataset used to access the PDF and FCS of the subsystem magnetization along one axis can also be used to measure it along any arbitrary direction. We next consider the transverse magnetization  $S_A^z$ . The Néel

state, for an even number of sites in the subsystem, is an eigenstate of  $S_A^z$  with zero eigenvalue; therefore, we expect the corresponding PDF to be  $p_z(q) = \delta_{q,0}$ . Since the transverse magnetization is well defined in the initial state and is globally conserved by the post-quench Hamiltonian, it does not change in the full system but it fluctuates within a subsystem during the time evolution, as seen in Fig. 1 (e). Here, we present the outcome probabilities in a measurement of  $S_A^z$  at different times. The dotted lines are the theoretical probabilities and the symbols and error bars are the experimental data. In the experimental data at time  $t = 0$  in panel (a) (the gray points), we notice that  $p_z(q = \pm 2) > 0$  whereas  $p_z(q = 0) < 1$ . Such mismatch of the ideal theory and the experimental result can be explained by taking into account the errors in the state preparation and in the measurements. At  $t = 0$ , these errors appear in the final measured bit-strings as random local bit-flips. Therefore, instead of the local qubit state being  $\rho_j^{\text{ideal}} = |\uparrow\rangle\langle\uparrow|$  or  $|\downarrow\rangle\langle\downarrow|$ , we can model the realized state as  $\rho_j^{\text{realized}} = (1 - p_j)\rho_j^{\text{ideal}} + p_j\sigma_j^x\rho_j^{\text{ideal}}\sigma_j^x$ . Here,  $p_j$  is the bit-flip rate at the  $j$ -th qubit, which is given by  $p_j = (1 - |\langle\sigma_j^z\rangle|)/2$ . We can estimate this rate in our experiment obtaining  $\langle\sigma_j^z\rangle$  from the classical shadows of the reduced density matrix. Utilizing these learned bit-flip rates, in Fig. 1 (e), we plot as dashed curves  $p_z(q)$  and  $p_z(q, t)$  for the initially realized state,  $|\Psi_0\rangle = \otimes_j \rho_j^{\text{realized}}$ , and observe a good match between the theory and the experiment.

Next, in Figs. 1 (f) and (g), the FCS  $\chi_z(\alpha)$  for the magnetization  $S_A^z$  is measured. At  $t = 0$  and even sized subsystems, the FCS is  $\chi_z(\alpha) = 1$ , represented by the dotted gray line in the plots. In the measured FCS, however, we see a different behavior, as shown in the figure with symbols and error bars. This is attributed to the same bit-flip errors as described above. The FCS in the prepared initial state is modified as  $\chi_z(\alpha) = \prod_j (\cos \alpha + i(1 - 2p_j) \sin \alpha) \prod_{j'} (\cos \alpha - i(1 - 2p_{j'}) \sin \alpha)$ , where  $j(j')$  runs over even (odd) indexed lattice sites. Once we include the sources of errors, the theory predictions (dashed curves) perfectly explain the measured data. We can see that the bit-flip errors become less relevant as time passes, and the difference between the FCS in a quench from the Néel state and a quench from the realized state reduces. Also note that as time passes the curvature of the real part of the FCS increases, which is reflected in an increasingly wide PDF, whereas the very small imaginary part of FCS corresponds to a near symmetric PDF at all times, as seen in Fig. 1 (e). The behavior of the FCS as a function of time is presented in Appendix D.

*Case II: Probability distribution function and full counting statistics in the quench dynamics from a tilted ferromagnetic state–* We now consider the other class of initial states; namely, the tilted ferromagnets (4). These states were realized in the recent experiment [64], on a system of  $N = 12$  qubits. These states make an interesting example because their distributions are distinct

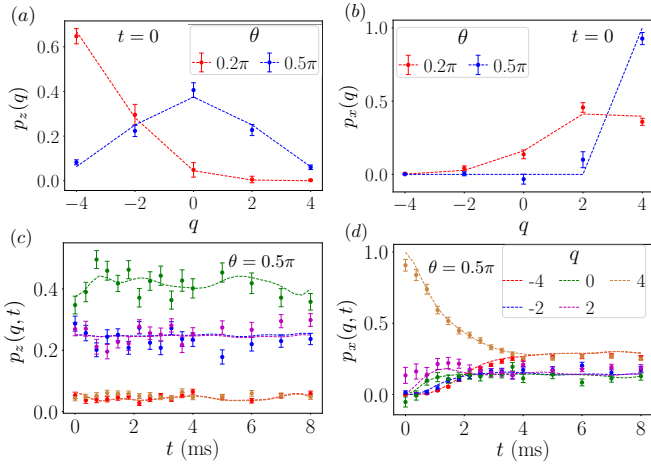


FIG. 2: *Magnetization probability distribution functions in the quench from tilted ferromagnetic states:* We present measurements of the PDF in a system of  $N = 12$  sites and subsystem of size  $N_A = 4$ , for two of the magnetizations,  $S_A^z$  (panels (a) and (c)) and  $S_A^x$  (panels (b) and (d)). The dashed curves are the theoretical predictions, obtained including the experimental errors during the quench dynamics, whereas the dots and error bars show the experimental data. (a,b) The PDFs are shown as functions of the possible measurement outcomes  $q$  for two choices of the tilt angle  $\theta = 0.2\pi$  and  $0.5\pi$  at the initial time. (c,d) We plot the PDFs during the quench dynamics for several values of  $q$  for an initial tilted ferromagnet with  $\theta = 0.5\pi$ .

from that of a Néel state. In Fig. 2 (a), we present the outcome probabilities in the measurement of  $S_A^z$  for a subsystem of  $N_A = 4$  qubits centered in the chain, and two choices of the rotation angle,  $\theta = 0.2\pi$  and  $0.5\pi$ , at time  $t = 0$ . For  $\theta = 0.5\pi$ , we theoretically expect  $p_z(q, \theta = 0.5\pi) = 2^{-N_A} \binom{N_A}{(N_A - q)/2}$ , which corresponds to the blue curve in Fig. 2 (a). The red curve is the theoretical PDF  $p_z(q)$  for the angle  $\theta = 0.2\pi$ . In Fig. 2 (b), we show the PDF for the longitudinal magnetization  $S_A^x$  at  $t = 0$ . For  $\theta = 0.5\pi$ , we expect that  $p_x(q, \theta = 0.5\pi) = \delta_{N_A - q, 0}$ , which corresponds to the blue dashed curve in the figure, whereas we notice some deviation in the experimental data. This can be both an artifact of the choice of the subsystem and an effect of the measurement errors (see Appendix F). As the tilting angle  $\theta$  decreases, the PDF  $p_x(q)$  becomes wider and its peak is displaced towards  $q = 0$ , as happens for the dashed red curve in the figure, which corresponds to  $\theta = 0.2\pi$ .

In Figs. 2 (c) and (d), we show the time evolution of the PDF for  $S_A^z$  and  $S_A^x$ , respectively, after the quench from a tilted ferromagnet with  $\theta = 0.5\pi$ . Their dynamics show different behavior as discussed in the following. While for the  $z$  component,  $p_z(q)$  is an even function in  $q$  and remains almost constant in time for all the possible values of the magnetization, this is not the case in the  $x$

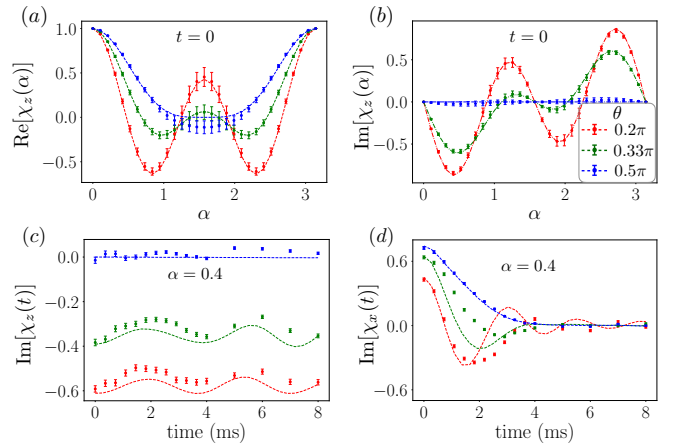


FIG. 3: *Magnetization full counting statistics in the quench from tilted ferromagnetic states:* We utilize the data from the Ref. [64] to measure the magnetization FCS in a system of  $N = 12$  sites and subsystem of size  $N_A = 4$ . The dashed curves are the numerical results in the presence of experimental errors, and the dots and error bars show the measurement data. (a-b) Real and imaginary parts of the FCS  $\chi_z(\alpha)$  for the magnetization  $S_A^z$  at initial time  $t = 0$  as functions of the spectral parameter  $\alpha$ . We see different behavior for different tilt angles  $\theta$  (red-  $0.2\pi$ , green-  $0.33\pi$ , blue-  $0.5\pi$ ), in agreement with the results for the PDFs obtained in Fig. 2 (see main text). (c-d) Imaginary part of the FCS  $\chi_\mu(t)$  for the transverse magnetization ( $\mu = z$ ) and for the longitudinal magnetization ( $\mu = x$ ) under the quench with the Hamiltonian (3). Again, the time evolution of the imaginary FCS is consistent with the results for the time-evolved PDFs reported in Fig. 2.

magnetization. As we see in panel (d), when  $t = 0$ ,  $p_x(q)$  is only non-zero for  $q = 4$ . After the quench,  $p_x(q = 4)$  decreases until it becomes stationary at late time, around  $t \approx 4$  ms. On the other hand, the probabilities of the rest of the allowed values of  $q$  increase under the time evolution. In particular, the probability of  $q = -4$  saturates to the same value as that for  $q = 4$  at a similar time. The probabilities for  $q = -2, 0$  and  $2$  reach simultaneously the same stationary value around  $t = 2$  ms. Therefore, at large times,  $p_x(q)$ , which is initially a delta function, becomes symmetric under  $q \mapsto -q$ . All this phenomenology is well captured by the experimental data. In the theoretical curves for the time evolution, in addition to the Hamiltonian unitary evolution, we have incorporated possible sources of experimental errors.

In connection to the measurements of the magnetization PDF in tilted ferromagnets, in Fig. 3 we show the experimental results for the corresponding FCS  $\chi_\mu(\alpha)$ . In all of the four panels in the Fig. 3, we take three values of the initial tilt angle,  $\theta = 0.2\pi$  (in red),  $0.33\pi$  (in green), and  $0.5\pi$  (in blue). We see that the experimental data points (dots and error bars) follow the theory predictions (dashed curves) thus providing a good estimation of the

FCS in the quantum simulator. The calculation of the error bars is detailed in the Appendix E.

For the states  $|\Psi_0(\theta)\rangle$ , at  $t = 0$ , the FCS is  $\chi_z(\alpha) = (\cos \alpha - i \sin \alpha \cos \theta)^{N_A}$ , and  $\chi_x(\alpha) = (\cos \alpha + i \sin \alpha \sin \theta)^{N_A}$ . In Figs. 3 (a) and (b), we present measurements of the real and imaginary parts of  $\chi_z(\alpha)$ . In panel (b), we see that the imaginary FCS, near  $\alpha = 0$ , is smallest for the largest of the three angles and it increases in magnitude with the decreasing angle. This observation is consistent with the symmetry of the PDF in Fig. 2 (a), i.e., the PDF is symmetric for the angle  $0.5\pi$  and asymmetric for the angle  $0.2\pi$ . Moreover, the negative slope of the imaginary FCS for  $\theta = 0.2\pi$  at  $\alpha = 0$  indicates a negative value of the mean of the corresponding PDF  $p_z(q)$ , cf. the red curve in Fig. 2 (a). Another physically interesting value of the FCS is  $\alpha = \pi/2$ . As we see in Fig. 3 (a), its real part exhibits a peak at that point when  $\theta = 0.2\pi$ , which becomes smaller as  $\theta$  increases and disappears for  $\theta = 0.5\pi$ . At  $\alpha = \pi/2$ ,  $\chi_\mu(\alpha)$  is the expectation value,  $\chi_\mu(\pi/2) = i^{N_A} \langle P_\mu \rangle$ , of the spin parity operator  $P_\mu = \prod_{j \in A} \sigma_j^\mu$  in the  $\mu$  axis. For the tilted ferromagnet,  $\langle P_\mu \rangle$  is the component of the spins in the  $\mu$  axis; in particular,  $\langle P_z \rangle = (-\cos \theta)^{N_A}$ . This explains the behavior of the peak at  $\alpha = \pi/2$  observed in Fig. 3 (a). For the behavior of  $\chi_x(\alpha = \pi/2)$ , see Appendix D 3.

The symmetry of the PDF during the time evolution can further be related to the measurements of the time evolved FCS. In Figs. 3 (c) and (d), the imaginary parts of the FCS along the  $z$  and the  $x$  directions as functions of the quench time  $t$  are shown. We see that  $\text{Im}[\chi_z(t)]$  nearly remains constant with time in contrast to the time evolution of  $\text{Im}[\chi_x(t)]$  which approaches zero at late times. We can compare the results for the tilt angle  $0.5\pi$  with those obtained for the corresponding PDF in Figs. 2 (c) and (d). The nearly zero value of the  $\text{Im}[\chi_z(t)]$  during the evolution (the blue curve in the Fig. 3(c)) is consistent with the symmetry  $p_z(-q) = p_z(q)$  for all  $t$ , as in the Fig. 2 (c). On the other hand, the late time symmetrizing behavior of  $p_x(q, t)$  in Fig. 2(d), is manifested in the late time relaxation of  $\text{Im}[\chi_x(t)]$  to a zero value.

*Conclusions and outlook*– In this letter, we have presented measurements of the full counting statistics (FCS) and the probability distribution function (PDF) of observables in subsystems of extended quantum systems prepared in a trapped-ion quantum simulator. We reanalyzed the experimental data from two previous experiments where quantum quenches with a long-range Ising type Hamiltonian (Eq. (3)) have been performed. Using the first experiment [63], we presented our results for the FCS and PDF of the subsystem magnetization in a system of 10 qubits prepared initially in a Néel state. Using the second experiment [64], we have studied the magnetization FCS and PDF in a system of 12 qubits prepared initially in tilted ferromagnets (see Eq. (4)).

The key ingredient in our work has been the post-processing of the experimental data measured in random bases. Such measurements allow the reconstruction of shadows of the realized density matrices of subsys-

tems of interest within the whole system. The possibility to access expectation values in an arbitrary subsystem makes our measurement protocol versatile. At the same time, the protocol allows access to the FCS and PDFs of any operator independent of them being symmetries of the evolution Hamiltonian (as is the requirement in many of the analytic techniques used to calculate FCS). Such efficiency of the protocol makes our measurement scheme useful in characterizing the prepared quantum states along all possible magnetization directions.

Although we have focused the current demonstration on a 1D chain using a trapped-ion quantum simulator, our measurement scheme can be directly adapted to other quantum platforms where single-site controls and detections are feasible. Note that, the theory of randomized measurements finds interesting applications in higher dimensions, as has already been demonstrated in a recent remarkable experiment studying thermalization [77]. FCS in 1D and beyond is a useful tool to distinguish quantum phases [78] and studying thermalization [39]. Therefore, having these protocols open up new directions especially when we lack the theoretical tools to analyze time-dependent quantum fluctuations.

*Acknowledgements*– LKJ acknowledges support from the European Union’s Horizon Europe program under the Marie Skłodowska Curie Action Project ETHOQS (Grant no. 101151139). PC and FA acknowledge support from ERC under Consolidator Grant number 771536 (NEMO) and from European Union - NextGenerationEU, in the framework of the PRIN Project HIGHEST no. 2022SJCKAH\_002. MKJ and CFR acknowledge the funding under Horizon Europe programme HORIZON-CL4-2022-QUANTUM-02-SGA via the project 101113690 (PASQuanS2.1).

## APPENDICES

### A. Properties of the FCS and PDFs

The FCS (1) and the PDF (2) are related by the Fourier transform

$$\chi(\alpha) = \sum_q p(q) e^{i\alpha q}. \quad (5)$$

If we take the Taylor expansion of the FCS  $\chi(\alpha)$  around  $\alpha = 0$ ,

$$\chi(\alpha) = 1 + i\alpha \langle O_A \rangle - \frac{1}{2} \alpha^2 \langle O_A \rangle^2 + \dots, \quad (6)$$

then we can see that its real and imaginary parts correspond to the even and odd powers in  $\alpha$  respectively. This means that, if  $\chi(\alpha)$  is real, then it is an even function in  $\alpha$  and, according to Eq. (5), yields a PDF  $p(q)$  symmetric in  $q$ , i.e.  $p(q) = p(-q)$ . Therefore, the imaginary part of  $\chi(\alpha)$  informs us about how asymmetric is the PDF with respect to  $q = 0$ . In particular, its leading order term in

the expansion around  $\alpha = 0$  is the mean  $\mu = \langle O_A \rangle$  of the corresponding PDF. In combination with the quadratic term of the real part, we can also determine its variance,  $\sigma^2 = \langle O_A^2 \rangle - \langle O_A \rangle^2$ . Therefore, a larger positive (negative) slope of  $\text{Im}(\chi(\alpha))$  at  $\alpha = 0$  indicates that the PDF has a larger positive (negative) mean. When the mean is small,  $\mu \approx 0$ , we can approximate the variance as  $\sigma^2 \approx \langle Q_A^2 \rangle$ . In that case, a larger curvature of  $\text{Re}(\chi(\alpha))$  at  $\alpha = 0$  tell us that the corresponding PDF has a larger variance.

Both  $\langle O_A \rangle$  and  $\langle O_A^2 \rangle$  can be extracted from the randomized measurement data. Therefore, the mean  $\mu$  and the variance  $\sigma^2$  can in principle be determined without resorting to the knowledge of the FCS. However, the calculation of  $\sigma^2$  using  $\sigma^2 = \langle O_A^2 \rangle - \langle O_A \rangle^2$  suffers from catastrophic cancellation: a very good approximation of  $\langle O_A \rangle$  and  $\langle O_A^2 \rangle$  may yield a very bad approximation of  $\sigma^2$  if both terms are of the same order of magnitude. The FCS might provide a solution to this issue as the leading order term of its logarithm around  $\alpha = 0$ ,

$$\log \chi(\alpha) = i\mu\alpha - \frac{1}{2}\sigma^2\alpha^2 + \dots \quad (7)$$

gives direct access to  $\sigma^2$ .

In the case of the magnetization,  $\alpha = 0$  is not the only point of  $\chi(\alpha)$  that provides physically relevant information. Taking into account that  $e^{i\alpha\sigma_j^\mu} = \cos(\alpha)I + i\sin(\alpha)\sigma_j^\mu$ , we have that  $\alpha = \pi/2$  is the expectation value  $\chi_\mu(\pi/2) = i^{N_A}\langle P_\mu \rangle$  of the spin parity operator  $P_\mu = \prod_{j \in A} \sigma_j^\mu$  in the  $\mu$  axis. In particular, if the subsystem  $A$  is in a product state with all the spins aligned with the  $\mu$  axis, then  $\langle P_\mu \rangle = (-1)^{n_\mu^-}$  where  $n_\mu^-$  is the number of spins pointing in the negative direction of  $\mu$ . In the tilted Néel state, since all the spins are aligned with the  $z$  axis, we have that  $\langle P_z \rangle = 1$  and  $\langle P_x \rangle = 0$  for an even number of ions in  $A$ . This explains why in Fig. 1, the FCS vanishes at  $\alpha = \pi/2$  for the longitudinal magnetization but not for the transverse one. Observe that  $\langle P_z \rangle$  is strongly affected by the bit-flip errors in the state preparation and by the time evolution, being very close to zero at  $t = 4$  ms. On the other hand,  $\langle P_x \rangle$  exhibits only minor oscillations around zero throughout the entire time evolution. In the tilted ferromagnetic state, the spins have certain component both in the  $z$  and  $x$  directions and, therefore,  $\langle P_z \rangle = (-\cos\theta)^{N_A}$  and  $\langle P_x \rangle = (\sin\theta)^{N_A}$ .

## B. Classical shadows and measurement estimators

We use classical shadows to estimate the FCS and PDF. After the state  $\rho(t)$  is prepared, projective measurements are performed in random bases. This is achieved by applying local random rotations  $U = \otimes_i u_i$ , where  $u_i$  are drawn from a unitary 2-design, to reach the state  $U\rho(t)U^\dagger$ . On this state, projective measurements in the computational  $z$ -basis are performed. For the same set of  $u_i$ , the experiment is repeated to collect  $N_M$

projections in the  $z$ -basis. At each measurement, we obtain the bitstrings  $s_i^{(r,m)}$ , where the site index  $i$  runs in the interval  $i = 1, \dots, N_A$  and  $m = 1, \dots, N_M$ . The experiment is repeated for  $N_u$  choices of random unitaries, collecting  $N_M$  projections for each random  $U$ . Thus for  $r$ -th set of random unitaries at a local site  $i$ , the measurement shots are  $\mathbf{s}_i^{(r)} = \{s_i^{(r,1)}, s_i^{(r,2)}, \dots, s_i^{(r,N_M)}\}$ . These data sufficiently provide the shadow of the reduced density matrix for the  $r$ -th random unitary.

The classical shadow  $\hat{\rho}_A^{(r)}$  of the density matrix  $\rho_A$  is constructed by averaging over the shadows  $\hat{\rho}_A^{(r,m)}$  of the  $N_M$  measured bitstrings for an applied unitary  $U^{(r)}$ ,  $\hat{\rho}_A^{(r)} = \mathbb{E}_{N_M}[\hat{\rho}_A^{(r,m)}]$ , where each of the  $\hat{\rho}_A^{(r,m)}$  is [65, 66]

$$\hat{\rho}_A^{(r,m)} = \bigotimes_{i \in A} 3U_i^{(r)\dagger} \left| s_i^{(r,m)} \right\rangle \left\langle s_i^{(r,m)} \right| U_i^{(r)} - \mathbb{I}_2. \quad (8)$$

The classical shadows form an unbiased estimator of the density matrix of interest, that is, the average over the applied unitaries and the measurement outcomes gives  $\mathbb{E}[\hat{\rho}_A^{(r,m)}] = \rho_A$ .

Our estimator for FCS uses the shadows  $\hat{\rho}_A^{(r)}$  to obtain the estimator

$$\hat{\chi}(\alpha) = \frac{1}{N_u} \sum_{r=1}^{N_u} \text{Tr} \left[ \hat{\rho}_A^{(r)} e^{i\alpha O_A} \right], \quad (9)$$

such that  $\mathbb{E}[\hat{\chi}(\alpha)] = \chi(\alpha)$ . Similarly, the estimator for the corresponding PDF reads

$$\hat{p}(q) = \frac{1}{N_u} \sum_{r=1}^{N_u} \text{Tr} \left[ \hat{\rho}_A^{(r)} \Pi_q \right] \quad (10)$$

such that  $\mathbb{E}[\hat{p}(q)] = p(q)$ . Note that, since the random unitaries  $U^{(r)}$  are uniformly distributed, these estimators are agnostic to the spatial orientation of the observable  $O_A$  considered, allowing to obtain the FCS and PDF of globally conserved as well as globally non-conserved operators with the same measurement data.

## C. Measurements of $\langle S_A^x \rangle$ and $\langle (S_A^x)^2 \rangle$ in a quenched Néel state

For a complementary understanding of the FCS, in the Fig. 4 we have presented the components  $\langle S_A^x \rangle$ ,  $\langle (S_A^x)^2 \rangle$ ,  $\langle S_A^z \rangle$ , and  $\langle (S_A^z)^2 \rangle$  as functions of time. The values  $\langle S_A^x \rangle$ ,  $\langle S_A^z \rangle$  correspond directly to the mean of the corresponding PDF and the slope of the imaginary FCS. Alongside, the values  $\langle (S_A^x)^2 \rangle$ ,  $\langle (S_A^z)^2 \rangle$  with time denote the changes in the curvature of the real part of the FCS as functions of time.

## D. FCS and PDF as functions of time

For completeness of results, in this section we show the measurements of the FCS and PDF as functions of

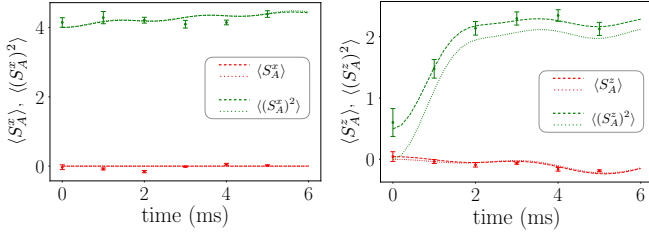


FIG. 4: In a quenched Néel state, measurements of expectation of the longitudinal magnetization and its squared (left panel), and that of transverse magnetization and its squared (right panel) are shown. The dotted curve show ideal theory whereas the dashes include initial state preparation and measurement errors. The system comprises of  $N = 10$  qubits with subsystem  $A$  sized  $N_A = 4$ .

time. These are the complementary figures to the ones presented in the main text.

### 1. PDF vs. time for Néel state

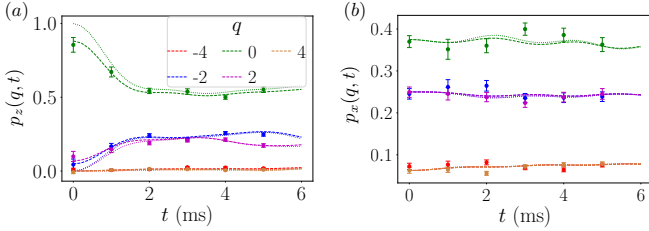


FIG. 5: In a system of  $N = 10$  qubits and  $N_A = 4$  sized subsystem, the probability distribution function of the operator  $S_A^z$  (panel (a)) and that of the operator  $S_A^x$  (panel (b)) as a function of time are shown. The measured data (dots and error bars) closely follow the theory prediction (as in dashed curves).

We have studied the PDF in a quench dynamics from a Néel state in the main text. We present in Fig. 5 the time evolution of the PDFs  $p_x(q, t)$  and  $p_z(q, t)$ . We notice, as also observed in Fig. 1 in the main text, that the PDF of the  $x$  magnetization changes very little with time satisfying  $p(q) = p(-q)$  at all times. On the other hand, the PDF of the subsystem magnetization in the  $z$  direction fluctuates significantly with time.

### 2. FCS vs. time for Néel state

The time evolution of the magnetization FCS for a Néel state after a quench with the XY Hamiltonian is presented in Fig. 6. In panels (a) and (b), the real and imaginary parts of the FCS  $\chi_z(\alpha)$  of the magnetization operator  $S_A^z$  is shown, comparing the measured data and the theoretical curves. As in the main text,

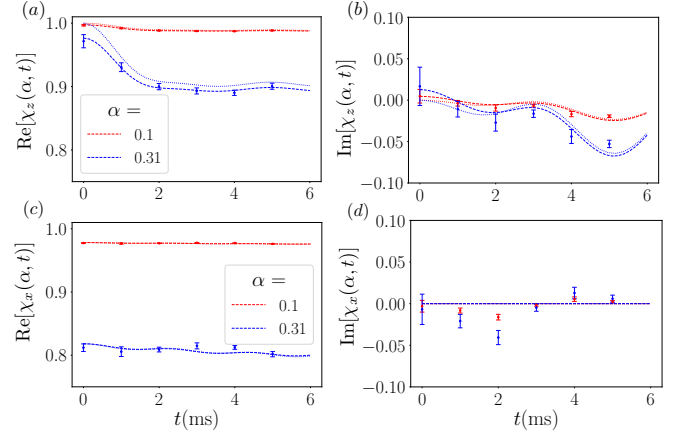


FIG. 6: In a system of  $N = 10$  qubits and  $N_A = 4$  sized subsystem, the full counting statistics for operators  $S_A^z$  (top row) and  $S_A^x$  (bottom row) are shown as a function of quenching time. The results are shown for two choices of the spectral parameter  $\alpha$ . The measured data (dots and error bars) closely follow the theory prediction (as in dashed curves) drawn for the error corrected initial Néel state.

we note that the experimental data slightly deviate from the ideal theory (the dotted curves) during the time evolution. However, once we include the state preparation and measurement errors in the theory calculations, the curves (dashes) agree with the experimental data. In panels (c) and (d), we measure the real and imaginary parts of the FCS  $\chi_x(\alpha)$  for the magnetization  $S_A^x$ . The very small deviations from the ideal theory are within the allowed error due to finite measurement budget. The near zero value of the  $\text{Im}[\chi_x]$  at all times is consistent with the symmetry of the PDF  $p_x(q)$ , as already observed in Fig. 5.

### 3. More on the FCS for tilted ferromagnetic state

In Figs. 7(a) and (b), we present the FCS at the initial time  $t = 0$  for the operator  $S_A^x$  and three tilting angles,  $\theta = 0.2\pi$ ,  $0.33\pi$  and  $0.5\pi$ . The set up is the same as in Figs. 3 (a-b), where we carry out the same analysis but for the operator  $S_A^z$ . Observe that, as in that case,  $\chi_x(\alpha)$  has a peak at  $\alpha = \pi/2$ , but now it shows the opposite behavior: it is bigger for  $\theta = 0.5\pi$  than for  $\theta = 0.33\pi$  and  $0.2\pi$ . As discussed in Appendix A, the reason is that  $\chi_x(\pi/2)$  corresponds to the expectation value of the spin parity operator and, for a tilted ferromagnet, coincides with the component of the spins in the  $x$ -axis,  $\chi_x(\pi/2) = i^{N_A} (\sin \theta)^{N_A}$ .

The time evolution of the real part of the FCS for the operators  $S_A^x$  and  $S_A^z$  during the quench dynamics is presented in Figs. 7 (c) and (d), respectively, complementing Figs. 3 (c) and (d), where we plotted the corresponding imaginary parts. In the  $z$ -axis, as also happens with the

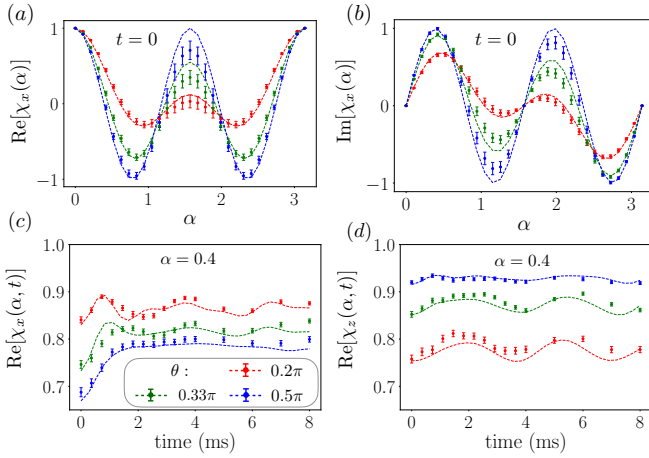


FIG. 7: At the initial time  $t = 0$ , for the operator  $S_A^x$  and three tilting angles,  $\theta = 0.2\pi$ ,  $0.33\pi$  and  $0.5\pi$ , we present the FCS vs.  $\alpha$  in the top row. In the bottom row, the measurement of the real part of the FCS for the operators  $S_A^x$  and  $S_A^z$  as a function of time is presented for the three angles.

imaginary part, it remains almost constant in time for any  $\theta$ . This is consistent with Fig. 2 (c) where we found that the corresponding PDF for  $\theta = 0.5\pi$  only oscillates after the quench. On the other hand, for the longitudinal magnetization, the real part of the FCS initially grows after the quench and eventually saturates around  $t = 2$  to a stationary value, different for each angle  $\theta$  analyzed. This contrasts with the imaginary part, cf. panel (d) of Fig. 3, which converges to zero for any  $\theta$ .

### E. Experimental parameters and error analysis

The experiment in Ref. [63] begins with a Néel state in a system of  $N = 10$  ions and then a quantum quench with the XY Hamiltonian is performed. In the present work, we have used this experimental data without any change. The experiment was performed with  $N_u = 500$  random rotations and  $N_M = 150$  shots per random rotation. The experiment beginning with the tilted ferromagnetic states in Ref. [64] is done on a system of  $N = 12$  ions. The experiment is performed with  $N_u = 500$  random rotations and  $N_M = 30$  shots per random rotation. The experiment also employs the XY Hamiltonian for the quench and we use the data provided without any change.

In the main text, the error bars of the PDFs are the standard error of the mean over  $N_u$  random unitaries. For the FCS, the error bars show the propagation of errors due to the form of the FCS as a function of the parameter  $\alpha$ , see below.

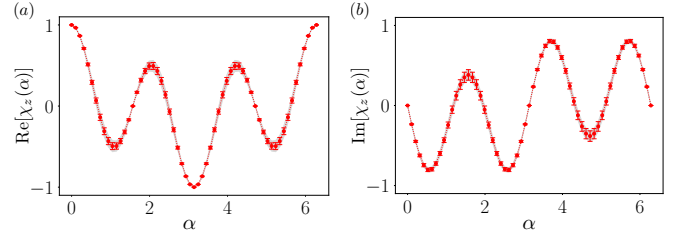


FIG. 8: Real and imaginary parts of FCS for a system with  $N = 12$ ,  $N_A = 3$  and tilting angle  $\theta = 0.2\pi$ . Red dots and error bars show direct estimation as presented in the main text. Shaded region shows the experimental measurements using the expanded expression as in Eqns. (13)-(16).

#### 1. Error propagation in measurements of full counting statistics

Considering the example of the longitudinal magnetization operator  $O_A = S_A^z = \sum_{j=1}^{N_A} \sigma_j^z$ , its full counting statistics is

$$\chi_z(\alpha) = \text{Tr} \left( \rho_A \prod_j e^{i\alpha\sigma_j^z} \right) \quad (11)$$

Expanding this we get,

$$\begin{aligned} \chi_z(\alpha) &= \text{Tr}[\rho_A \prod_j (\cos \alpha + i\sigma_j^z \sin \alpha)] \\ &= \text{Tr}[\rho_A ((\cos \alpha)^{N_A} + i(\cos \alpha)^{N_A-1} \sin \alpha \sum_{j=1}^{N_A} \sigma_j^z \\ &\quad - (\cos \alpha)^{N_A-2} (\sin \alpha)^2 \sum_{\substack{j,j'=1 \\ i < j}}^{N_A} \sigma_j^z \sigma_{j'}^z \\ &\quad + \dots + (i)^{N_A} \sigma_1^z \sigma_2^z \dots \sigma_{N_A}^z (\sin \alpha)^{N_A} )]. \quad (12) \end{aligned}$$

The errors are correctly estimated using the propagation of uncertainties. Explicitly, taking as example a subsystem of size  $N_A = 3$ , we have

$$\begin{aligned} \text{Re}[\chi_z(\alpha)] &= -\cos(\alpha) \sin^2(\alpha) (\langle \sigma_1^z \sigma_2^z \rangle + \langle \sigma_2^z \sigma_3^z \rangle + \langle \sigma_1^z \sigma_3^z \rangle) \\ &\quad + \cos^3(\alpha), \quad (13) \end{aligned}$$

and

$$\begin{aligned} \text{Im}[\chi_z(\alpha)] &= \cos^2(\alpha) \sin(\alpha) (\langle \sigma_1^z \rangle + \langle \sigma_2^z \rangle + \langle \sigma_3^z \rangle) \\ &\quad - \sin^3(\alpha) \langle \sigma_1^z \sigma_2^z \sigma_3^z \rangle. \quad (14) \end{aligned}$$

The corresponding errors are

$$\begin{aligned} \eta(\text{Re}[\chi(\alpha)]) &= \cos(\alpha) \sin^2(\alpha) (\eta(\sigma_1^z \sigma_2^z)^2 + \eta(\sigma_2^z \sigma_3^z)^2 + \eta(\sigma_1^z \sigma_3^z)^2)^{1/2} \quad (15) \end{aligned}$$



and

$$\eta(\text{Im}[\chi(\alpha)]) = (\sin^3 \alpha \eta(\sigma_1^z \sigma_2^z \sigma_3^z)^2 + \cos^2 \alpha \sin \alpha (\eta(\sigma_1^z)^2 + \eta(\sigma_2^z)^2 + \eta(\sigma_3^z)^2))^{1/2}, \quad (16)$$

where  $\eta(O)$  denotes the error in the estimation of the observable  $O$ . Note that, the above expression is strictly valid for a completely independent measurement of each term in the expansion. In the Fig. 8, we take an example of a system of  $N = 12$  spins prepared in an initially tilted ferromagnetic state  $|\Psi_0(\theta = 0.2\pi)\rangle = e^{i\theta \sum \sigma_j^y / 2} |\downarrow \downarrow \dots\rangle$ , and use the data from the experiment to measure the FCS. The red dots and error bars are obtained using the direct estimation as presented in the main text, whereas the shaded region is drawn using the formulas presented in this appendix, using the same data set to obtain quantities like,  $\langle \sigma_1^z \rangle$ ,  $\langle \sigma_1^z \sigma_2^z \rangle$  etc. We notice that our formulas correctly capture the qualitative behavior of the error bars propagation as a function of  $\alpha$ . Note also that, due to an odd subsystem size  $N_A = 3$ , the periodicity of FCS is at  $\alpha = 2\pi$  instead of  $\alpha = \pi$  as seen in the main text for  $N_A = 4$ .

#### F. Average probabilities

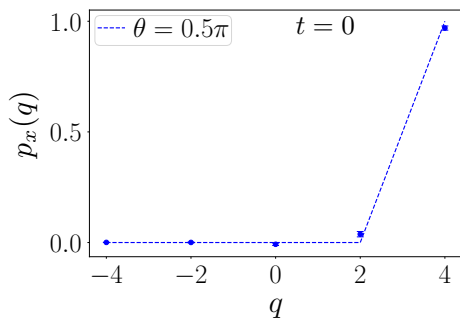


FIG. 9: Average probabilities in a measurement of  $S_A^x$  in the subsystems for a tilted ferromagnetic state at angle  $\theta = 0.5\pi$ .

To reduce statistical error, we can consider taking the average over all bulk subsystems. As an example, in the Fig. 9, we see the measurement of the PDF  $p_x(q)$  at  $t = 0$  for the tilted ferromagnetic state  $|\Psi(\theta = 0.5\pi)\rangle$ . We notice, compared to the PDF for a single interval presented in the main text, the statistical errors are significantly reduced. However there is still some measurement error. This error is difficult to model since the experimental measurements are tailored to specific measurement basis, with focus to reduce local  $z$ -rotations during measurements. Nevertheless the measurement sequence is performed uniformly to realize the Haar random unitaries.

- 
- [1] Y. M. Blanter and M. Buttiker, *Phys. Rep.* **336**, 1 (2000).
  - [2] C. Gardiner and P. Zoller, “Quantum noise: A handbook of markovian and non-markovian quantum stochastic methods with applications to quantum optics,” (Springer-Verlag Berlin Heidelberg, 2004).
  - [3] Y. V. Nazarov, “Quantum noise in mesoscopic physics,” (Springer Dordrecht, 2012).
  - [4] W. E. Lamb and R. C. Retherford, *Phys. Rev.* **72**, 241 (1947).
  - [5] R. Bellwied, S. Borsányi, Z. Fodor, S. D. Katz, A. Pásztor, C. Ratti, and K. K. Szabó, *Phys. Rev. D* **92**, 114505 (2015).
  - [6] M. Herrero-Collantes and J. C. Garcia-Escartin, *Rev. Mod. Phys.* **89**, 015004 (2017).
  - [7] S. K. Lamoreaux, *Reports on Progress in Physics* **68**, 201 (2005).
  - [8] S. Hofferberth, T. S. I. Lesanovsky, A. Imambekov, V. Gritsev, E. Demler, and J. Schmiedmayer, *Nature Phys.* **4**, 489 (2008).
  - [9] J. Armijo, T. Jacqmin, K. V. Kheruntsyan, and I. Bouchoule, *Phys. Rev. Lett.* **105**, 230402 (2010).
  - [10] T. Jacqmin, J. Armijo, T. Berrada, K. V. Kheruntsyan, and I. Bouchoule, *Phys. Rev. Lett.* **106**, 230405 (2011).
  - [11] M. Gring, M. Kuhnert, T. Langen, T. Kitagawa, B. Rauer, M. Schreitl, I. Mazets, D. A. Smith, E. Demler, and J. Schmiedmayer, *Science* **337**, 1318 (2012).

- [12] J. G. Bohnet, B. C. Sawyer, J. W. Britton, M. L. Wall, A. M. Rey, M. Foss-Feig, and J. J. Bollinger, *Science* **352**, 1297 (2016).
- [13] M. Rispoli, A. Lukin, R. Schittko, S. Kim, M. E. Tai, J. Leonard, and M. Greiner, *Nature* **573**, 385 (2019).
- [14] R. W. Cherng and E. Demler, *New J. Phys.* **9**, 7 (2007).
- [15] M. Bortz, J. Sato, and M. Shiroishi, *J. Phys. A: Math. Theor.* **40**, 4253 (2007).
- [16] D. B. Abraham, F. H. L. Essler, and A. Maciolek, *Phys. Rev. Lett.* **98**, 170602 (2007).
- [17] A. Lamacraft and P. Fendley, *Phys. Rev. Lett.* **100**, 165706 (2008).
- [18] D. A. Ivanov and A. G. Abanov, *Phys. Rev. E* **87**, 022114 (2013).
- [19] V. Eisler, *Phys. Rev. Lett.* **111**, 080402 (2013).
- [20] I. Klich, *J. Stat. Mech.* , P11006 (2014).
- [21] M. Moreno-Cardoner, J. F. Sherson, and G. D. Chiara, *New J. Phys.* **18**, 103015 (2016).
- [22] K. Najafi and M. Rajabpour, *Phys. Rev. B* **96**, 235109 (2017).
- [23] J.-M. Stéphan and F. Pollmann, *Phys. Rev. B* **95**, 035119 (2017).
- [24] M. Collura, F. H. L. Essler, and S. Groha, *J. Phys. A* **50**, 414002 (2017).
- [25] A. Bastianello, L. Piroli, and P. Calabrese, *Phys. Rev. Lett.* **120**, 190601 (2018).
- [26] A. Bastianello and L. Piroli, *J. Stat. Mech.* , 113104 (2018).
- [27] M. Arzamasovs and D. Gangardt, *Phys. Rev. Lett.* **122**, 120401 (2019).
- [28] M. N. Najafi and M. A. Rajabpour, *Phys. Rev. B* **101**, 165415 (2020).
- [29] P. Calabrese, M. Collura, G. D. Giulio, and S. Murciano, *EPL* **129**, 60007 (2020).
- [30] F. Ares, M. Rajabpour, and J. Viti, *Phys. Rev. E* **103**, 042107 (2021).
- [31] K.-L. Cai and M. Cheng, [arXiv:2401.09548](https://arxiv.org/abs/2401.09548) .
- [32] V. Eisler and Z. Rácz, *Phys. Rev. Lett.* **110**, 060602 (2013).
- [33] I. Lovas, B. Dóra, E. Demler, and G. Zaránd, *Phys. Rev. A* **95**, 053621 (2017).
- [34] S. Groha, F. H. L. Essler, and P. Calabrese, *Sci. Post Phys.* **4**, 043 (2018).
- [35] M. Collura, *Sci. Post Phys.* **7**, 072 (2019).
- [36] O. Gamayun, O. Lychkovskiy, and J.-S. Caux, *Sci. Post Phys.* **8**, 036 (2020).
- [37] R. J. Valencia-Tortora, P. Calabrese, and M. Collura, *EPL* **132**, 50001 (2020).
- [38] B. Bertini, P. Calabrese, M. Collura, K. Klobas, and C. Rylands, *Phys. Rev. Lett.* **131**, 140401 (2023).
- [39] R. Senese, J. H. Robertson, and F. H. L. Essler, *SciPost Phys.* **17**, 139 (2024).
- [40] R. F. E. Tirrito, A. Santini and M. Collura, *SciPost Phys.* **15**, 096 (2023).
- [41] B. Bertini, K. Klobas, M. Collura, P. Calabrese, and C. Rylands, *Phys. Rev. B* **109**, 184312 (2024).
- [42] D. X. Horvath and C. Rylands, *Phys. Rev. A* **109**, 043302 (2024).
- [43] D. X. Horvath, B. Doyon, and P. Ruggiero, [arXiv:2411.14406](https://arxiv.org/abs/2411.14406) .
- [44] N. Ranabhat and M. Collura, *SciPost Phys. Core* **7**, 017 (2024).
- [45] I. Klich and L. Levitov, *Phys. Rev. Lett.* **102**, 100502 (2009).
- [46] I. Klich and L. Levitov, *Adv. Theor. Phys.* **1134**, 36 (2009).
- [47] H. F. Song, C. Flindt, S. Rachel, I. Klich, and K. L. Hur, *Phys. Rev. B* **83**, 161408(R) (2011).
- [48] H. F. Song, S. Rachel, C. Flindt, I. Klich, N. Laflorencie, and K. L. Hur, *Phys. Rev. B* **85**, 035409 (2012).
- [49] P. Calabrese, M. Mintchev, and E. Vicari, *EPL* **98**, 20003 (2012).
- [50] G. C. Levine, M. J. Bantegui, and J. A. Burg, *Phys. Rev. B* **86**, 174202 (2012).
- [51] R. Susstrunk and D. A. Ivanov, *EPL* **100**, 60009 (2012).
- [52] P. Calabrese, P. L. Doussal, and S. N. Majumdar, *Phys. Rev. A* **91**, 012303 (2015).
- [53] Y. Utsumi, *Eur. Phys. J. Spec. Top.* **227**, 1911 (2019).
- [54] M. Goldstein and E. Sela, *Phys. Rev. Lett.* **120**, 200602 (2018).
- [55] J. C. Xavier, F. C. Alcaraz, and G. Sierra, *Phys. Rev. B* **98**, 041106 (2018).
- [56] A. Lukin, M. Rispoli, R. Schittko, M. E. Tai, A. M. Kaufman, S. Choi, V. Khemani, J. Leonard, and M. Greiner, *Science* **364**, 6437 (2019).
- [57] F. Ares, S. Murciano, and P. Calabrese, *Nature Comms.* **14**, 2036 (2023).
- [58] C. Rylands, K. Klobas, F. Ares, P. Calabrese, S. Murciano, and B. Bertini, *Phys. Rev. Lett.* **133**, 010401 (2024).
- [59] J. F. Wienand, S. Karch, A. Impertro, C. Schweizer, E. McCulloch, R. Vasseur, S. Gopalakrishnan, M. Aidelsburger, and I. Bloch, *Nature Physics* (2024).
- [60] Google AI and collaborators, *Science* **384**, 48 (2024).
- [61] D. Wei, A. Rubio-Abadal, B. Ye, F. Machado, J. Kemp, K. Srakaew, S. Hollerith, J. Rui, S. Gopalakrishnan, N. Y. Yao, I. Bloch, and J. Zeiher, *Science* **376**, 716 (2022).
- [62] A. Valli, C. P. Moca, M. A. Werner, M. Kormos, Z. Kraljnik, T. Prosen, and G. Zaránd, [arXiv:2409.14442](https://arxiv.org/abs/2409.14442) .
- [63] T. Brydges, A. Elben, P. Jurcevic, B. Vermersch, C. Maier, B. P. Lanyon, P. Zoller, R. Blatt, and C. F. Roos, *Science* **364**, 260 (2019).
- [64] L. K. Joshi, J. Franke, A. Rath, F. Ares, S. Murciano, F. Kranzl, R. Blatt, P. Zoller, B. Vermersch, P. Calabrese, C. F. Roos, and M. K. Joshi, *Phys. Rev. Lett.* **133**, 010402 (2024).
- [65] H.-Y. Huang, R. Kueng, and J. Preskill, *Nat. Phys.* **16**, 1050 (2020).
- [66] A. Elben, S. T. Flammia, H.-Y. Huang, R. Kueng, J. Preskill, B. Vermersch, and P. Zoller, *Nat. Rev. Phys.* **5**, 9 (2023).
- [67] A. Rath, R. van Bijnen, A. Elben, P. Zoller, and B. Vermersch, *Phys. Rev. Lett.* **127**, 200503 (2021).
- [68] K. J. Satzinger, Y.-J. Liu, A. Smith, C. Knapp, *et al.*, *Science* **374**, 1237 (2021).
- [69] J. C. Hoke, M. Ippoliti, E. Rosenberg, *et al.*, *Nature* **622**, 481 (2023).
- [70] A. Rath, V. Vitale, S. Murciano, *et al.*, *PRX Quantum* **4**, 010318 (2023).
- [71] Y. Zhou, P. Zeng, and Z. Liu, *Phys. Rev. Lett.* **125**, 200502 (2020).
- [72] A. Elben, R. Kueng, H.-Y. R. Huang, R. van Bijnen, C. Kokail, M. Dalmonte, P. Calabrese, B. Kraus, J. Preskill, P. Zoller, and B. Vermersch, *Phys. Rev. Lett.* **125**, 200501 (2020).
- [73] A. Neven, J. Carrasco, V. Vitale, C. Kokail, A. Elben, M. Dalmonte, P. Calabrese, P. Zoller, B. Vermersch,

- R. Kueng, and B. Kraus, *npj Quantum Inf.* **7**, 152 (2021).
- [74] M. K. Joshi, A. Elben, B. Vermersch, T. Brydges, C. Maier, P. Zoller, R. Blatt, and C. F. Roos, *Phys. Rev. Lett.* **124**, 240505 (2020).
- [75] L. K. Joshi, A. Elben, A. Vikram, B. Vermersch, V. Galitski, and P. Zoller, *Phys. Rev. X* **12**, 011018 (2022).
- [76] H. Dong, P. Zhang, C. B. Dag, Y. Gao, N. Wang, J. Deng, X. Zhang, J. Chen, S. Xu, K. Wang, *et al.*, *arXiv preprint arXiv:2403.16935* (2024).
- [77] T. I. Andersen, N. Astrakhantsev, A. Karamlou, J. Berndtsson, J. Motruk, A. Szasz, J. A. Gross, T. Westerhout, Y. Zhang, E. Forati, *et al.*, *arXiv preprint arXiv:2405.17385* (2024).
- [78] C.-Y. Wang, T.-G. Zhou, Y.-N. Zhou, and P. Zhang, *Phys. Rev. Lett.* **133**, 083402 (2024).